AIAA 2002-3026
CFD Simulation of Laser Ablation Carbon Nanotube Production

R. Greendyke
The University of Texas at Tyler
Tyler, Texas

C. Scott
NASA JSC
Houston, Texas

J. Swain
The University of Texas at Tyler
Tyler, Texas

CFD SIMULATION OF LASER ABLATION CARBON NANOTUBE PRODUCTION

R.B. Greendyke[1]
The University of Texas at Tyler
Tyler, Texas

C.D. Scott[2]
NASA Johnson Space Center
Houston, Texas

J. Swain[3]
The University of Texas at Tyler
Tyler, Texas

Abstract

The production of carbon nanotubes and fullerenes by laser ablation has been an ongoing process at NASA-Johnson Space Center for several years now. The mechanisms of nanotube production are not well understood and a conventional CFD simulation code (VULCAN) is applied to the study of the flowfield dynamics and chemical kinetics of nanotube production. A simple 12-species, 14-reaction model for the formation of carbon molecules up to C_6 has been incorporated into the code. Simulations of the plume resulting from a single 10 ns laser pulse are used for the analysis of flowfield dynamics and chemical concentrations using C_6 as an 'indicator species' for fullerene production. An additional dual laser pulse simulation was conducted to mimic actual production techniques. Both cases were run to a simulated post ablation time of 8 milliseconds. Thermal profiles appear to exceed those of experimental observations, although this comparison might be erroneous. Flowfield dynamics yield good agreement with the available limited experimental data for most of the simulation. C_6 production remained nearly constant despite diffusion of other species into the background argon.

Introduction

While production of carbon nanotubes has successfully taken place for some time now by a variety of methods including arc-jet ablation of carbon, laser ablation of carbon, and chemical vapor deposition, little is understood about the exact chemical kinetics and processes involved in the formation of carbon nanotubes. In addition, most of the research into the production of single-walled carbon nanotubes (SWNT) has been of an experimental nature that does not in and of itself yield theoretical chemical kinetics models. NASA-Johnson Space Center has recently devoted a large degree of effort into the production of SWNT via the laser-ablation method first developed by Smalley, et al. at Rice University [1]. As a necessary precursor for any direct chemical kinetic modeling of the formation and production of SWNT, or improvement of the production methodology, it is necessary to first understand the basic flow dynamics of the processing of nanotubes in the laser-ablation oven facility at NASA Johnson Space Center.

Fig. 1 shows a basic schematic of the laser-ablation oven at NASA-JSC. Construction of the facility is simple in concept. Two concentric quartz tubes of 1.5 mm thickness form the inner and outer tubes with inside diameters of 2.2 and 5.08 cm respectively. At one end of the inner tube are located two 10 Hz pulsed lasers operating at 1064 nm and 532 nm wavelength with beam diameters of 5 mm aligned coaxially with the longitudinal axis of the inner quartz tube. For standard nanotube production runs, a 10 ns 532 nm pulse is followed 50 ns later by a 10 ns 1064 nm pulse. Each pulse is of 300 mJ energy. A target of carbon graphite with nickel and cobalt catalysts

---

[2] is located at the other end of the inner quartz tube.

A "base" flow of 100 sccm of argon is maintained from the laser location and exits past the carbon target at a pressure of 66.7 kPa. These conditions yield a baseline mass flow through the chamber of 2.723×10^{-6} kg/s of argon. The whole oven facility is heated to a temperature of 1473 K prior to nanotube production runs. Upon laser irradiation, part of the carbon target ablates immediately and forms a carbon vapor "plume" that injects into the argon base flow towards the laser initially at supersonic velocities.

The primary task of this investigation will be to study the basic flow dynamics and thermophysics of the carbon plume as it progresses through the flow chamber in the first 8 milliseconds after laser ablation. Insight into the chemical reactions inherent in carbon nanotube production will also be gained. Previous studies [3-4] indicated that the flow is primarily in the inner quartz tube with the area between the inner and outer tubes, as well as the flow past the sting-mounted carbon target being of little consequence in primary plume development in the ablation process. These regions of flow have been ignored in this study as a consequence. In addition, a simplified version of the carbon 'buckyball' reaction kinetics model of Krestinin and Moravsky [5] has been included in this study for the purpose of determining the effect of primary carbon nanotube 'building block' formation on the flowfield and thermophysics of the simulation (it is speculated that carbon nanotubes are primary formed from C_2, C_3, and other simplified carbon species). The chemical kinetics model will be examined in the next section.

Methodology

The mixed nature of the flow conditions (both supersonic carbon and near-quiescent argon) present in this study necessitated the use of a very flexible CFD code for analysis of the flow conditions. The VULCAN (Viscous Upwind aLgorithm for Complex flow ANalysis) code [6] developed at NASA Langley Research Center was selected for the simulation. Primarily developed for hypersonic propulsion applications, the VULCAN code has physical modeling capabilities that include chemically reacting flow, algebraic and PDE turbulence models, as well as multi-block capabilities in three-dimensional, two-dimensional, and axisymmetric fashion to name a few features.

The Hypersonic Airbreathing Propulsion Branch at NASA-LaRC supplied version 4.2.0 of the VULCAN code to the first author.

For the simulations at hand, it was determined that the axisymmetric version of the VULCAN code would be appropriate. Previous studies [3-4] had indicated that little flow dynamics takes place outside the inner quartz laser ablation tube and therefore the only computational domain used for this study was the 2.2 cm inner diameter tube. Gridding was accomplished by use of the Grid Generator add-on to the TECPLOT graphics software [7]. In order to compare with experimental data, grid point locations were assigned at 0.5 mm increments, corresponding to the minimum resolution of NASA-JSC's optical equipment. Experimental analysis [8] of the plume dynamics has indicated that little of the ablative carbon plume penetrates into the background argon flow more than 10 cm upstream of the carbon target, however the first author's study [4] indicated that the upstream boundary for the flow has to be placed at least 55 cm upstream of the carbon target to avoid pressure wave interference effects from the propagating plume. The computational domain was then split into two regions – the primary flow region (Fig. 2) immediately in front of the carbon target and extending to 10 cm upstream with a radial distance of 1.1 cm, which is divided into node points at 0.5 mm increments. The secondary region of the domain is located at the 10 cm location and extends to the 55 cm upstream location with much coarser (1 cm) horizontal nodal spacing.

Carbon Ablation Surface Boundary Conditions

Little experimental information has been available for the boundary conditions at the surface of the laser ablation carbon target. The only known thermophysical quantity has been the carbon mass ablation rate of 1.6×10^{-6} gm/laser pulse. Previous studies [3-4] then assumed that the carbon mass was injected into the flowfield through the 10 ns duration of the laser pulse. Resulting simultaneous solution of both the ideal gas and the Clausius-Claperyon equations resulted in a density of 10.59 kg/m^3, a gas temperature of 5211 K, a vapor pressure of 377 atm., and a carbon injection velocity of 1898.9 m/s at the 5 mm diameter boundary condition corresponding to the ablating surface of the carbon target. The resulting propagating carbon plumes, however, exceeded the shock

front locations data gathered by Puretzky, et al. [8] past the 200 μs post-ablation time.

The current study assumes that the actual ablation time is 15 ns – the additional 5 ns worth of ejected ablation material coming after the termination of the laser pulse. The resulting solution of ideal gas and Clausius-Claperyon equations showed that while the temperature of the injected carbon was relatively insensitive to the additional ablation time (T=4950 K), the vapor pressure of the carbon plume dropped considerably to approximately 100 atm. The corresponding density was 1.039 kg/m^3, and the plume injection velocity rose to 5228 m/s. Chemical equilibrium was assumed at the ablation surface and the CHEMKIN [9] code was used to determine inlet carbon species mass fractions for C through C_5 (no data being available in CHEMKIN for C_6). C_3 and C_5 were found to be the dominant species at the ablation surface inlet with the mass fraction of C_3 being 0.463 and C_5 being .426. The next contributors to the inlet flow were C_2 and C_4 with species mass fractions of 0.044 and 0.059 respectively. The atomic carbon mass fraction was nearly negligible at 0.008.

Simplified Carbon Reaction Modeling

Krestinin and Moravsky's chemical kinetics model for fullerene production was modified and incorporated into the VULCAN code for simulation of the building blocks of carbon nanotubes. 12 species and 14 reactions mechanisms were used in the abbreviated version of the model. The included chemical species were argon, electrons, and carbon molecules from C to C_6 with some of the primary ions as well. Little data is available on any carbon species past C_5 in size until the actual C_{60} and C_{70} fullerenes. Due to this, much of the required input for the VULCAN code's chemical reactions and thermophysical properties, such as viscosity, were approximated or extrapolated from known data for simpler species. The chemical reactions and coefficients are presented in Tables 1 and 2.

Flowfield Solution Methodology

The solution methodology for the carbon nanotube ablation process was simple. The background argon flow was solved for in steady-state fashion with the assumption that the argon flow had been fully heated to the 1473 K temperature of the surrounding oven. No chemical reactions take place since the flow is solely argon at this point. Full Navier-Stokes viscous effects and k-ω turbulence models inherent in the VULCAN code were used in a multi-block configuration. Iteration on the downstream exiting argon static pressure boundary condition was required until the 2.723×10^{-6} kg/s mass flow rate of argon used in the nanotube production process was achieved.

Once steady-state conditions at the correct mass flow rate for argon were achieved, the flowfields were retained and used as restart files for the carbon plume simulations. The VULCAN code was restarted with a time-dependant Runge-Kutta flowfield solution method. Grid points corresponding to the 5 mm diameter laser beam were reset with the above carbon ablation boundary conditions for the laser plume. The reacting chemistry model was incorporated. The solution was allowed to progress for 15 ns with time steps set at 10^{-10} sec. At a simulated 15 ns into the solution the carbon injection boundary condition was 'turned off' and replaced by a standard wall boundary condition with a temperature set to 1773 K [10]. The plume was then solved for as it progressed down the quartz inner tube domain with the time-dependant Runge-Kutta method. Two separate flowfield situations were analyzed. The first was a single pulse ablation of the carbon surface to study basic plume propagation, and the second was a dual pulse ablation with the carbon injection boundary condition be used twice with a 60 ns gap between to simulated the actual method of carbon nanotube production. Both solutions were allowed to progress downstream until 8 milliseconds of simulated time had elapsed. Occasional increases in time step size were used as the flow settled down but never exceeded 10^{-7} s.

Results and Discussion

Due to required real mesh intervals in the primary grid, initial simulations at the onset of ablation required small time steps on the order of 10^{-10} seconds of simulated time. All solutions therefore required extensive CPU time, but were accomplished without incident.

Temperature and Pressure Profiles

The temperature contours for the single pulse laser ablation cases are shown in Figs. 3-7 at various points in post ablation time. The white circles in these and other figures indicate the

approximate location of the leading edge of the carbon plume according to Puretzky, et al. [8]. The initial temperature of the injected carbon ablation products is 4950 K, however, the carbon plume temperatures rapidly rise after injection due to the recombination of simpler carbon molecules, releasing more energy into the flow. Comparison of this data to Arepalli, et al. [10] indicates a higher temperature than was yielded from experimental data. In addition, Scott, et al. [11] note that the temperature of the plume is in the 3000 to 4000 K range. However, their temperature profiles were obtained from spectroscopic data analysis of the carbon plume vibrational bands, not direct measurement and this could induce some error. In addition, the temperature data was taken experimentally at later stages in the plume development at specific locations in the plume, not throughout the plume geometry. It should also be noted that Puretzky's locations for the leading edge of the shock front were obtained by laser induced fluorescence (LIF) of the C_2 and C_3 molecules and the data does not exactly match temperature profiles – the LIF being a function of both temperature and mass fractions of the C_2 and C_3 molecules as shall be shown later. Therefore, comparison to either mass or temperature profiles alone does not exactly correspond to data that can be obtained by CFD simulations directly. The temperature profiles obtained from the VULCAN code do match closely the distance of the leading edge of the plume obtained from Puretzky however until the 200 microsecond point of the simulation, and then peak temperature locations of the carbon plume rapidly exceed the Puretzky locations. The characteristic 'smoke ring' shape of the carbon plume observed by researchers [2,8,10] is realized in the current simulations.

A profile of the peak flowfield temperatures for both the dual and single pulse laser ablation simulations is presented in Fig. 8. After the initial injection, the temperatures for both cases rapidly rise as the carbon recombines, then start to fall of as the plume cools and expands. There is a secondary short rise in temperatures as the reflected pressure wave from the carbon plume reflects off the side-wall of the inner quartz tube and recompresses the plume. All temperatures then drop until the maximum temperature is now 1773 K found at the gas immediately near the post-ablation point boundary condition of 1773 K. The dual ablation case has correspondingly higher temperatures than the single plume case due to the increase in injected carbon ablation products from the secondary laser pulse and the resulting increase in recombination from the additional carbon.

Pressure profiles resulting from the single ablation case are presented in Figs. 9-13 for key points in the simulation time. The initial inlet plume is supersonic and rapidly expands in hemispherical fashion as would be expected. Fig. 10 clearly indicates the impingement of the pressure wave on the inner quartz wall of the simulated carbon ablation chamber. The pressure wave from the rapid ablation then reflects and compounds downstream as is shown in Figs. 11 through 13.

C_3 and C_6 Production Profiles

Figures 14 – 18 illustrate the production of C_3 for the single ablation case for comparison to the Puretzky data. Figs. 14, 15, and 16 show the initial development of C_3 in the carbon plume at the 1, 10 and 100 microsecond points of post-ablation simulated time. The white circles, again, illustrate the approximate location of the leading edge of the carbon plume resulting from LIF of the C_3 molecules. At the 1 millisecond point of the simulation the maximum concentration of C_3 is approximately 1.5 cm further upstream of the location provided by Puretzky. However, as the C_3 diffuses into the argon background flow, the location of the leading edge of peak C_3 concentration again corresponds to the location of Puretzky at the 8 millisecond point as seen in Fig. 18. One possible explanation for the discrepancy at the 1 millisecond point could be the diffusion coefficient data used by the authors for C_3 and indeed all the carbon molecules larger than atomic carbon. No data was available for the diffusivity of the higher species of carbon and the data for atomic carbon was simply extrapolated for this simulation. It is reasonable to expect that the larger carbon molecules would diffuse more slowly into the argon background flow due to their size alone than is indicated in these simulations.

Peak mass fractions for the entire simulated flowfield regime are presented in Fig. 19. As would be expected, C_3 concentrations for the dual pulse case exceed those of the single pulse case by an approximate factor of two through most of the simulated time. Initial mass fractions on the order of 10^{-1} rapidly lower to the order of 10^{-4} as the carbon plume expands and diffuses into the argon flow.

C_6 production contours are presented for the dual ablation case in Figs. 20 – 22 for the

100 microsecond, 1 millisecond, and 8 millisecond post-ablation points. The dual ablation contours are presented since this simulates the actual production techniques used for carbon nanotube production and it is of interest where and how the higher order species of carbon is formed in the laser ablation process. At 100 microseconds post-ablation time, the C_6 mass fractions are relatively high, but can barely be noticed in Fig. 20. The primary location of the C_6 production is on the surface of the carbon ablation target immediately to one side or the other of the ablation boundary points. The C_6 is forming on the cooler carbon surface next to the injected and hotter carbon plume. Fig. 21 clearly indicates that the C_6 species is primarily formed in the cooler regions of the carbon wake as it progresses upstream into the argon flow. At 8 milliseconds of post-ablation time, the C_6 concentrations have diffused into the argon flow and the areas of C_6 production become more difficult to observe. It is noted that the production of C_5 did not take place in the carbon plume wake, but at the leading edge of the plume. Therefore it cannot be assumed that all higher order carbon species will be produced in the carbon plume wake, but Fig. 21 certainly indicates that this is the primary location of production for at least C_6.

Fig. 23 shows the peak C_6 mass fraction concentrations as a function of post-ablation time in the flowfield as a whole. It should be noted that initial concentrations are relatively high as the carbon plume contacts the colder carbon surface near the ablation sight and then fall off as that carbon diffuses into the argon flowfield. The concentrations then begin to rise and the plume itself cools and the plume vortex, or 'smoke ring', rotates back upon itself. For the majority of the simulation, C_6 mass fractions remain relatively constant in the range between 10^{-12} and 10^{-13}. When compared to the initially higher concentrations of the other carbon species, as seen in Figs. 24-27, the other species have high initial concentrations and then fall off as the simulation progresses by multiple orders of magnitude as the simulation progresses. C_6 peak mass fractions, although starting off low, remain reasonably flat towards the end of the simulation runs despite the added diffusion into the argon flow.

Conclusions

CFD simulation of the carbon plume resulting from laser ablation for both the single laser pulse case (for flowfield and kinetic studies) and the dual laser pulse case (to simulate actual production techniques) was reasonably successful using the limited information about the higher order species of carbon in the 12 species, 14 reaction model incorporated into the VULCAN code. Two discrepancies were noted however. The first is the excessive temperatures relative to those observed in actual experiments. It does need to be noted that the temperatures observed through experimental analysis were estimates obtained through spectroscopic analysis of the vibrational Swan bands of the carbon C_2 alone however, and only at specific geometric locations – not the entire plume as will result form CFD analysis. Therefore, such direct comparison of experimental data to flowfield calculations is difficult and not necessarily valid at this point in time. This differs this analysis with reacting chemistry from earlier work by the first author [3] wherein only C_3 was used in plume simulation. In that study, it was assumed that C_3 was the only species and chemical reactions were frozen solely for the purposes of studying the flowfield dynamics of the carbon plume, not the thermochemical effects. However, that study resulted in a very favorable temperature comparison to the limited experimental data.

The second discrepancy is the failure of the flowfield data for C_3 and C_2 to match the LIF data of Puretzky's propagation of the plume leading edge at the 1 millisecond point in post ablation time. As noted in the previous section and through examination of the 8 millisecond point in Fig. 18 however, the leading edge of the highest concentration of C_3 (and similar results were obtained for C_2), matches the location of Puretzky's LIF data for the leading edge of the C_2 and C_3 in the plume. The earlier high concentration of C_3 having dissipated by the 8 millisecond point in time. The lack of adequate data for the diffusivity of C_2 and C_3 alone could account for this variation from experimental data.

Examination of the peak mass fraction data shown in Figs. 19 and 23-27 yields interesting themes. The first observation is the location of C_6 production within the plume. All observed C_6 production occurred at either the interface between the plume and a cooler wall, or in the plume wake itself – not directly within the plume. If C_6 is taken to be an 'indicator species' for the prediction of actual nanotube and buckyball formation, it can be concluded that most of the production of fullerenes and

nanotubes will occur at a much later time in the plume development than has been speculated upon. One caution would be that the higher temperatures in the cases studied in this paper might be delaying the production however – more work is required to determine if this is a boundary condition problem or a chemical reaction rate problem. It is noted though that the mass fractions of C_6 remained relatively constant throughout the simulation time while other species mass fractions declined by orders of magnitude in the latter stages of the simulation as the carbon ablation plume spread and diffused into the argon flow.

Further analysis of the thermochemical dynamics of the carbon plume is an ongoing project at the current time. A chemical model for fullerene production is being included into the VULCAN code and the preceding carbon plume simulations will be re-run for a much fuller chemistry model. It is anticipated however that computational loads for the 70 species model necessary for fullerene analysis will be excessive.

Acknowledgements

References

1. Guo, T., Nikolaev, P., Thess, A., Colbert, D.T., Smalley, R.E, "Catalytic Growth of Single-Walled Nanotubes by Laser Vaporization," *Chemical Physics Letters*, Vol. 243, No. 49, 1995.
2. Arepalli, S., Nikolaev, P., Holmes, W., Scott, C.D., "Diagnostics of Laser-Produced Plume Under Carbon Nanotube Growth Conditions," *Applied Physics A*, Vol. 70, No. 2, February 2000.
3. Greendyke, R.B., Scott, C.D., and Swain, J., "CFD Analysis of Laser-Ablation Carbon Nanotube Plume Flow Dynamics*,"* Annual APS March Meeting 2002, Indianapolis, IN, March, 2002.
4. Greendyke, R.B., " CFD Simulation of Carbon Nanotubes," (Hyman, W., Sickorez, D., Miller, M., and Tarkington, W., Editors), NASA Contractor Report on Grants NAG 9-39 and 9-54, Vol. 1, pp. 10-1 to 10-14, Summer, 2001.
5. Krestinin, A. V., and Moravsky, A. P., "Mechanisms of Fullerene Synthesis in the Arc Reactor," *Chem. Phy. Lett*., Vol. 286, pp. 479-484, 1998.
6. http://hapb-www.larc.nasa.gov/~jawhite/
7. http://www.amtec.com
8. Puretzky, A.A., Geohegan, D.B., Fan, X., and Pennycook, S.J., "Dynamics of Single-Wall Carbon Nanotube Synthesis by Laser Vaporization," *Applied Physics A*, Vol. 70, No. 2, February 2000.
9. http://www.ca.sandia.gov/chemkin/
10. Arepalli, S., personal communication
11. C.D. Scott, S. Arepalli, P. Nikolaev, and R.E. Smalley, "Growth Mechanisms for Single-Wall Carbon Nanotubes in a Laser-Ablation Process", *Applied Physics A*, Vol. 72, No. 5, 2001, pp. 573-580.
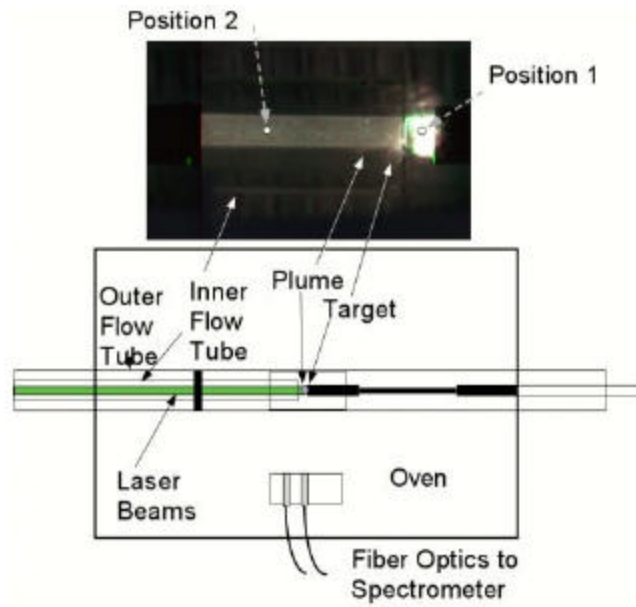
Figure 1. Schematic of NASA-JSC laser-ablation nanotube production oven.
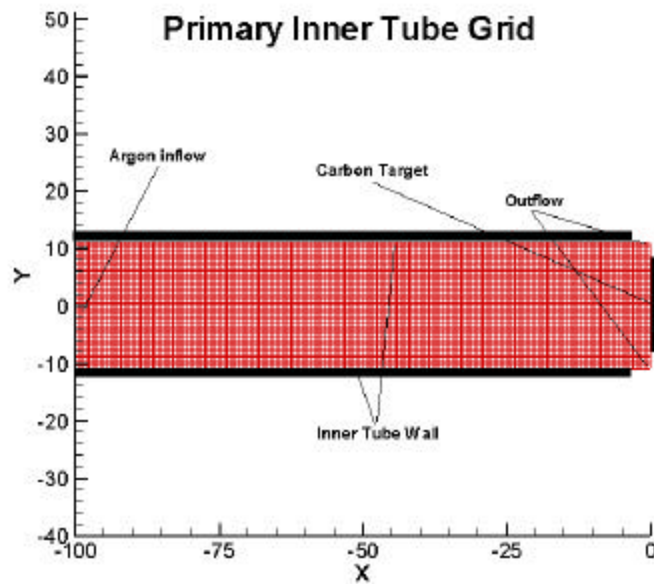
Figure 2. Computational grid for primary inner tube flowfield solution.
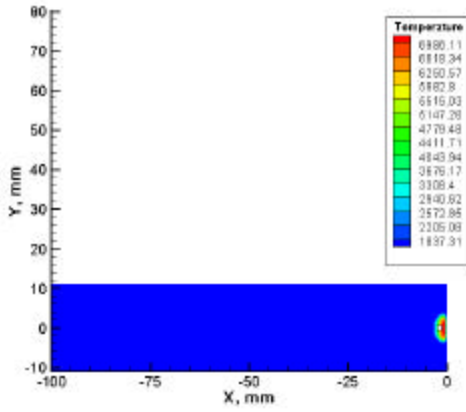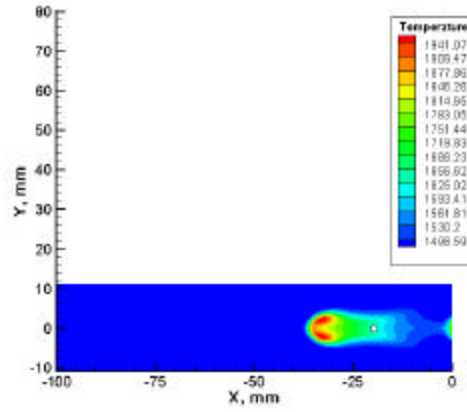
Figure 3. Temperature profiles at 1 microsec.

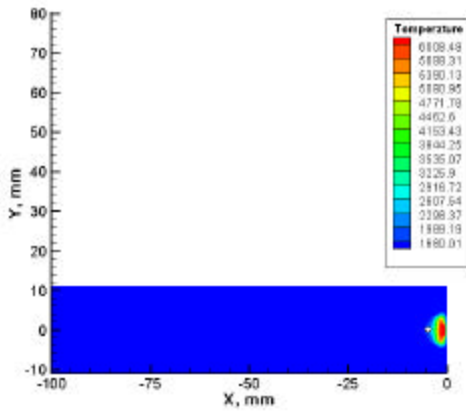**Figure 6. Temperature profiles at 1 millisec.**

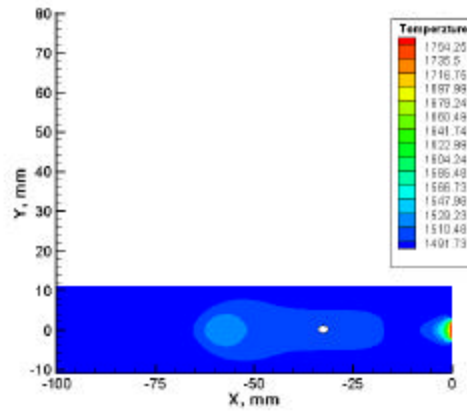**Figure 4. Temperature profiles at 10 microsec.**

Figure 7. Temperature profiles at 8 millisec.
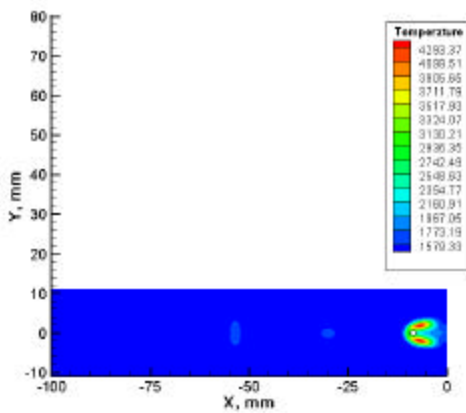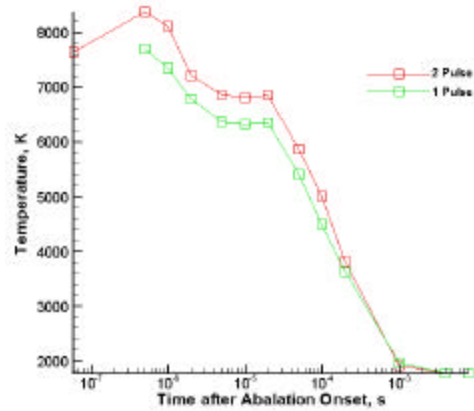

Figure 5. Temperature profiles at 100 microsec.

Figure 8. Peak temperature comparison between single and dual laser pulse ablation.
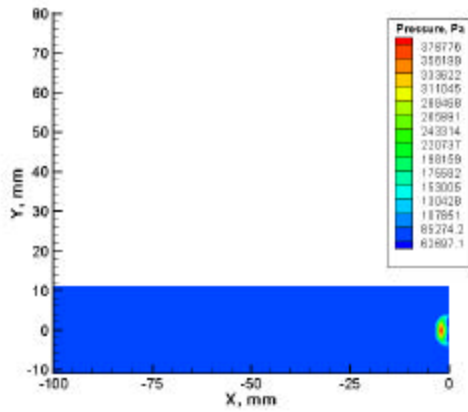
Figure 9. Pressure contours at 1 microsec.
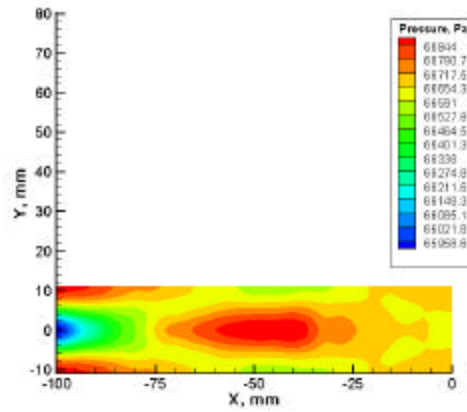
Figure 12. Pressure contours at 1 millisec.
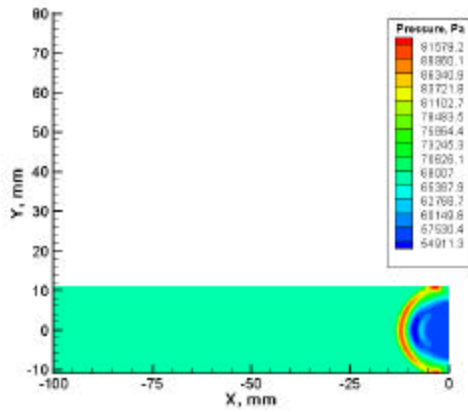
Figure 10. Pressure contours at 10 microsec.
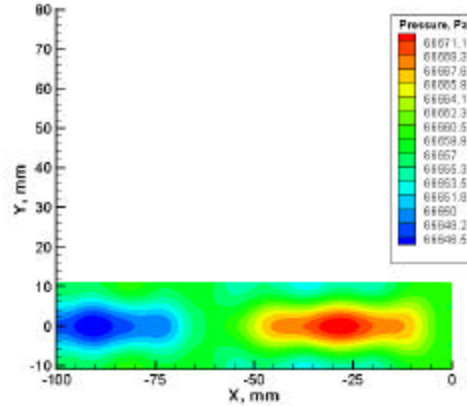
Figure 13. Pressure contours at 8 millisec.
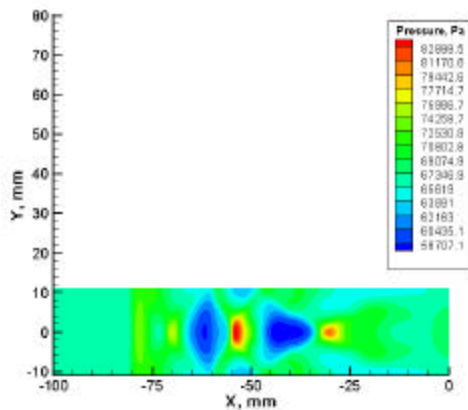
Figure 11. Pressure contours at 100 microsec.
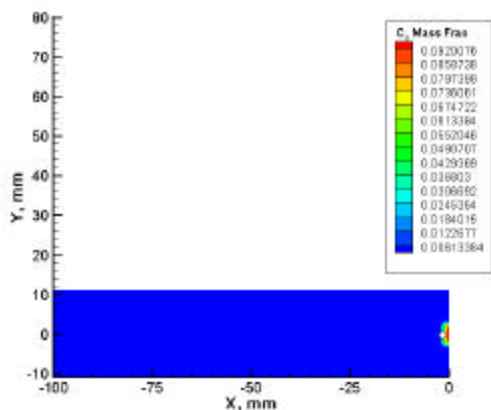
Figure 14. C3 mass fractions at 1 microsec.
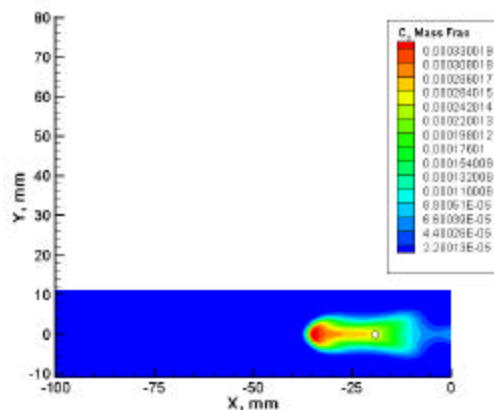
Figure 17. c3 mass fractions at 1 millisec.
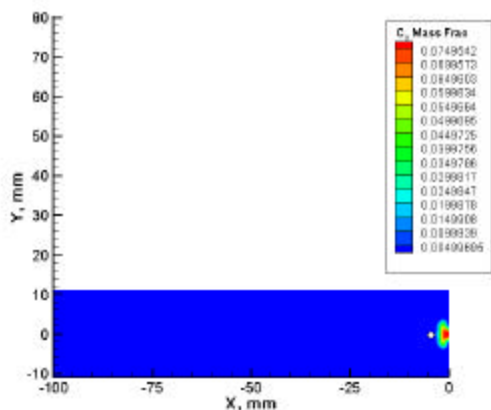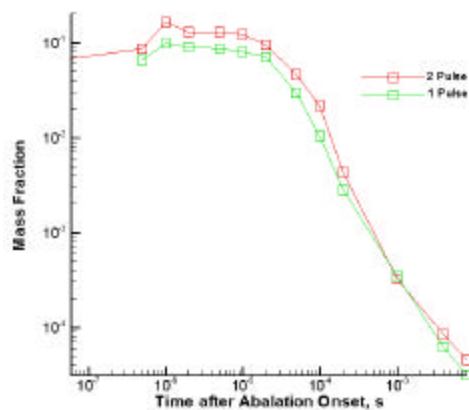

Figure 15. C3 mass fractions at 10 microsec.
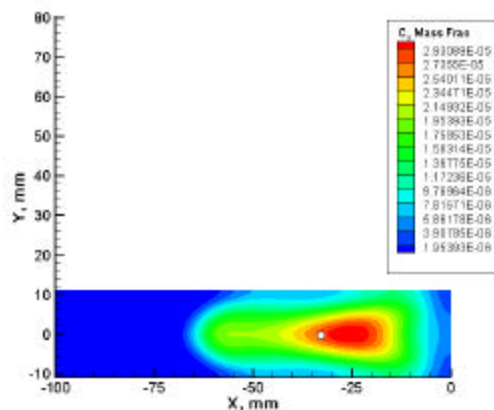
Figure 18. C3 mass fractions at 8 millisec.
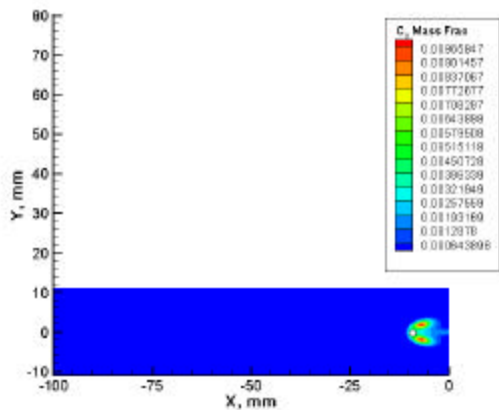
Figure 16. C3 mass fractions at 100 microsec.

Figure 19. Peak C3 mass fractions.
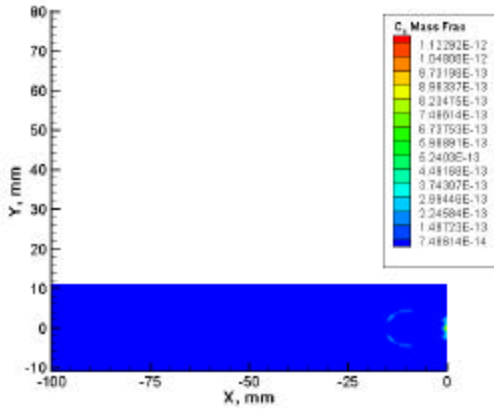
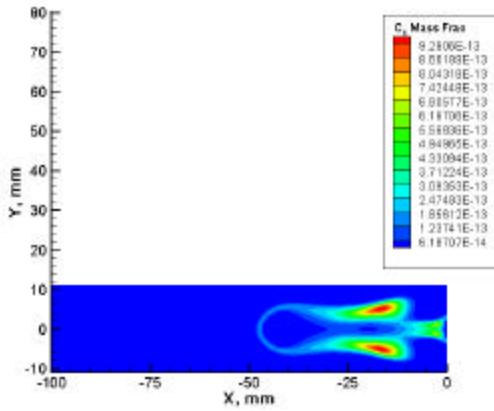**Figure 20. C6 mass fractions for dual pulse ablation at 100 microsec.**

Figure 21. C6 mass fractions for dual pulse ablation at 1 millisec.
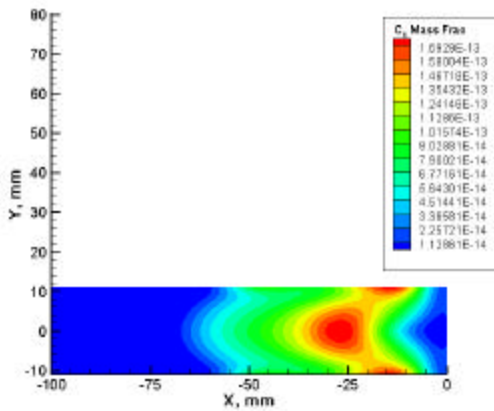

Figure 22. C6 mass fractions for dual pulse ablation at 8 millisec.
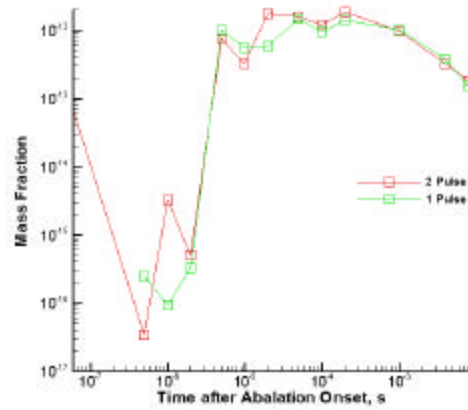

Figure 23. Peak C6 mass fractions as a function of post ablation time for both single and dual pulse laser ablation.
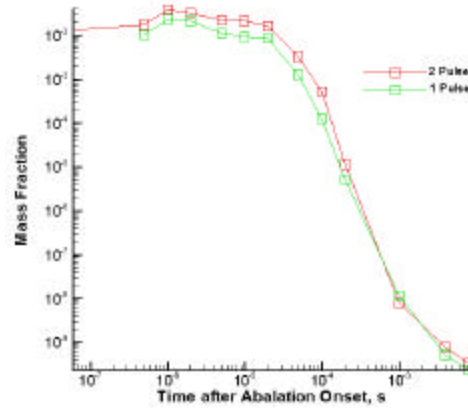

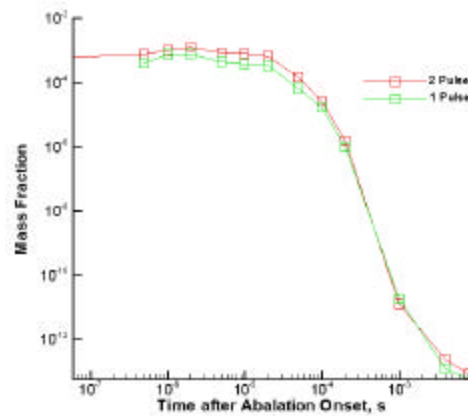**Figure 24. Peak C mass fractions as a function of post ablation time.**

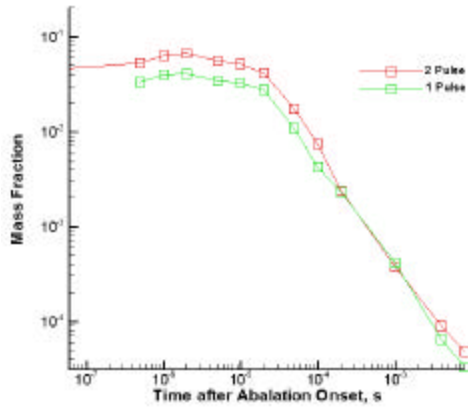**Figure 25. Peak C2 mass fractions as a function of post ablation time.**

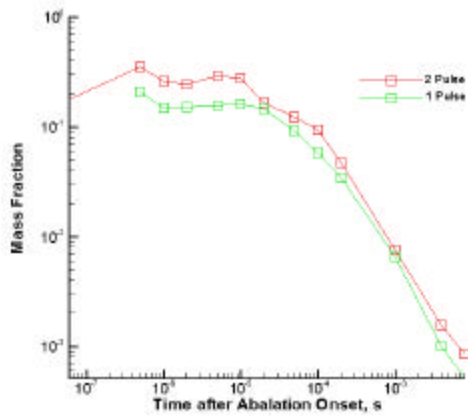**Figure 26. Peak C4 mass fractions as a function of post ablation time.**

Figure 27. Peak C5 mass fractions as a function of post ablation time.

Table 1. Simplified Carbon Chemistry Model

Reaction

1	$C + e^-$	$\Leftrightarrow$	$C^+ + e^- + e^-$
2	$C + C$	$\Leftrightarrow$	C_2
3	$C + C_2$	$\Leftrightarrow$	C_3
4	$C_2 + C_2$	$\Leftrightarrow$	$C_3 + C$
5	$C_2 + C_2$	$\Leftrightarrow$	C_4
6	$C + C_3$	$\Leftrightarrow$	C_4
7	$C + C_4$	$\Leftrightarrow$	C_5
8	$C_2 + C_3$	$\Leftrightarrow$	C_5
9	$C^+ + C_3$	$\Leftrightarrow$	C_4^+
10	$C^+ + C_4$	$\Leftrightarrow$	C_5^+
11	$C^+ + e^-$	$\Leftrightarrow$	C
12	$C_5 + C$	$\Leftrightarrow$	C_6
13	$C_4 + C_2$	$\Leftrightarrow$	C_6
14	$C_3 + C_3$	$\Leftrightarrow$	C_6

Table 2. Reaction Rate Coefficients (where $k_f=A*T^B*\exp(-T_a/T)$)

REACTION	A	B	Ta
1	5.46E-04	0.0	214420.0
2	2.00E+14	0.0	0.0
3	2.00E+14	0.0	0.0
4	2.00E+15	0.0	9040.0
5	2.00E+14	0.0	0.0
6	2.00E+14	0.0	0.0
7	2.00E+14	0.0	0.0
8	2.00E+14	0.0	0.0
9	9.00E+09	0.0	0.0
10	6.00E+14	0.0	0.0
11	3.60E+16	-4.5	0.0
12	2.00E+14	0.0	0.0
13	2.00E+14	0.0	0.0
14	2.00E+14	0.0	0.0